Role of nonlinearities and initial prepatterned surfaces in nanobead formation by ion-beam bombardment of Au(001): Experiments and theory

J.-H. Kim,[1] J.-S. Kim,[1,*] J. Muñoz-García,[2] and R. Cuerno[2,†]

[1]*Department of Physics, Sook-Myung Women's University, Seoul 140-742, Korea*

[2]*Departamento de Matemáticas and Grupo Interdisciplinar de Sistemas Complejos, Universidad Carlos III de Madrid, 28911 Leganés, Spain*

(Received 10 July 2012; revised manuscript received 15 October 2012; published 25 February 2013)

Au(001) surfaces that have been prepatterned into a rippled morphology develop one-dimensional nanodot arrays (nanobeads) selectively along the ripples when bombarded with energetic ions at an angle that is normal to the average surface orientation. By quantifying the shape and morphology of these arrays, we show experimentally and by numerical simulations of an extended Kuramoto-Sivashinsky equation that the degree of one-dimensional order of the nanobeads can be optimized by considering initial rippled surfaces with various wavelength and roughness values. Our simulations employ physical units and use the experimental topographies as initial conditions. Such nonideal shapes are key to elucidating the influence of nonlinear effects (like conformal interface motion and local redeposition) since the early stages of the dynamics for these prepatterned systems. In spite of the fact that the evolution of the surface morphology becomes far from trivial under these circumstances, our continuum model is able to reproduce the experimental results quantitatively, in contrast to relevant alternative models in the context of surface nanopatterning by ion-beam bombardment.

DOI: 10.1103/PhysRevB.87.085438 PACS number(s): 79.20.Rf, 81.16.Rf, 68.35.Ct, 05.45.−a

I. INTRODUCTION

For the last few decades, ion-beam sputtering (IBS) has proven to be a promising tool to fabricate highly ordered, nanoscale patterns on the surfaces of diverse materials via self-organization.[1–3] Under oblique incidence of the ion beam, for example, IBS fabricates periodic ripple patterns,[4] while under normal incidence it can generate hexagonal[5,6] or square-symmetric[7,8] patterns of dots or holes.

Development of such ordered patterns has been explained theoretically by a number of models. Bradley and Harper (BH) proposed a linear evolution equation for the height of the eroded target in which pattern formation by IBS results from counteracting processes such as roughening due to erosion by the ion beam and smoothening by diffusion of thus-created adatoms and vacancies.[9] This model reproduces some features of the ripple pattern,[2] although a number of nonlinear continuum equations were later introduced to improve upon its limitations.[7,10–12] Moreover, the interplay between sputtering and surface diffusion has been recently challenged experimentally as the main physical mechanism for pattern formation in targets such as semiconductors that become amorphous under irradiation.[13] Still, the BH mechanism is expected to dominate for metallic targets in the so-called erosive regime in which it is the ion beam, rather than crystalline anisotropies in surface diffusion, that controls the pattern formation process.[1,2]

Recently, multiple-ion-beam sputtering, in which two or more beams are projected onto the target surface, has been theoretically proposed to fabricate more sophisticated patterns via superposition of those produced by each ion beam.[14,15] Dual-ion-beam sputtering, the *simultaneous* projection of two ion beams at a grazing angle, but perpendicular to each other in azimuth, has been experimentally shown to generate square-symmetric patterns of nanodots/holes.[16] Also *sequential* ion-beam sputtering (SIBS) has been reported, in which the direction of an ion beam with respect to the surface is changed sequentially. Two types of SIBS have been examined; after forming an initial ripple pattern in one direction by sputtering at an oblique angle, the rippled surface is subsequently sputtered after changing the azimuthal angle by 90°,[17–19] or normal to the surface.[20] The patterns generated experimentally by SIBS disprove theoretical predictions[15] on the mere superposition of the patterns formed by each beam, although the latter has been observed in Monte Carlo simulations of discrete models of SIBS for an admittedly short simulation time window.[21]

Most of the experimental SIBS patterns[17–19] are similar to those that can be produced by a single beam. However, SIBS as in Ref. 20 does produce a novel nanostructure, such as a nanobead pattern, that is a highly ordered one-dimensional array of nanodots, formed along each initial ripple when these are subject to irradiation at normal incidence.[20] The nanobead morphology thus demonstrates the capability of SIBS to fabricate elaborate nanostructures via the sequential formation of basic patterns, in a form of hierarchical self-assembly.[22] This complex pattern formation process is driven by the competition of two length scales, namely, the wavelength of the initial ripple and the nanobead size. In particular, it provides a touchstone against which models of IBS nanopatterning can be examined. The extended Kuramoto-Sivashinsky (eKS) model[7,12] has been found to reproduce most of the observed experimental results, such as formation of the nanobead structure and its preservation during SIBS, in contrast to other models, such as the KS and BH equations.[20] Hence, the additional nonlinear effects present in the eKS model are found to be essential in order to explain the evolution of nanobead morphologies during SIBS.

In this work, we study experimentally and theoretically how the shape of the initial ripple pattern affects the formation and dynamics of the nanobead structure by IBS normal to the initial rippled surface. While in Ref. 20 a single rippled condition was explored, here we address the interplay between the two relevant length scales by performing experiments on

several different initial conditions. The degree of ordering, and thus the quality, of the nanobead structure is seen to depend on the properties of the initial surface. Nevertheless, for large enough ion doses, the morphologies become similar, largely independent of those features. An additional difference of the present work with respect to Ref. 20 is to perform simulations of the eKS model employing physical units and for a range of different nonflat initial conditions. This enables successful quantitative comparison with experiments and allows us to develop a unified picture of the process that self-consistently elucidates the observed temporal evolution of the nanobead patterns.

II. EXPERIMENTS

All our ion-beam-sputtering experiments have been carried out in a custom-built ultrahigh vacuum chamber with base pressure of about 5×10^{-10} Torr. For the fabrication of the initial ripple patterns, IBS was performed along the densely packed [110] direction of the Au(001) targets at a polar incidence angle of 72° with respect to the surface normal. The ion energy ε and partial pressure of Ar^+ P_{Ar} were 2 keV and 1.2×10^{-4} Torr, respectively, generating an ion flux $f \simeq 0.3$ ions nm^{-2} s^{-1}. The largest ion fluence achieved, defined as the ion flux multiplied by the total sputter time, was 4500 ions nm^{-2}. In order to vary the mean wavelength and roughness of the initial ripple pattern, we sputtered substrates at different temperatures (Table I), while keeping other conditions fixed. For higher substrate temperatures, the mean wavelength of the initial ripple pattern becomes larger. The temperature was measured by a K-type thermocouple slightly away from the sample and can be a little lower than the real one. *In situ* x-ray photoelectron spectroscopy (XPS) of sputtered Au samples reveals no traceable amount of contaminants, implying little unintended deposition of impurities by sputtering (figures not shown). The initial ripple patterns were then analyzed *ex situ* by an atomic force microscope (AFM) in the contact mode.

Table I summarizes the features of the rippled surfaces thus generated, such as the mean ripple wavelength λ_R^i and the global surface roughness or surface width W^i. Here, the superscript i refers to initial and the subscript R refers to the ripple pattern. The roughness $W(t)$ is defined as $W(t) \equiv \sqrt{\langle [h(\mathbf{r},t) - \overline{h}(t)]^2 \rangle}$, where $\overline{h}(t)$ is the mean height at time t and $\langle \cdot \rangle$ denotes the space average. The mean ripple wavelength λ_R was estimated as the distance from the central ripple to the neighboring one in the two-dimensional height-height correlation function $G(\mathbf{r},t)$, which is defined as $G(\mathbf{r},t) \equiv \langle h(\mathbf{r}_i,t) h(\mathbf{r}_i + \mathbf{r},t) \rangle$. For each experimental condition NB(a), NB(b), etc., values quoted in Table I for the various quantities are average results over more than ten samples.

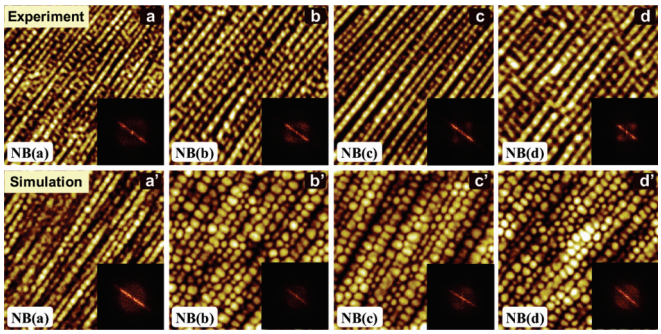

FIG. 1. (Color online) (top) Optimal nanobead patterns formed by IBS normal to the initial rippled surfaces in Table I: (a) NB(a), (b) NB(b), (c) NB(c), and (d) NB(d). The size of each image is 1×1 μm^2. (bottom) Nanobead patterns obtained by numerical simulations of Eq. (1) for corresponding experimental initial rippled surfaces. For each image, the inset provides the corresponding height power spectrum (squared modulus of the Fourier transform).

We subsequently sputtered each rippled surface at normal incidence. Arrays of nanobeads self-organize along each initial ripple. During this sputtering process, P_{Ar}, ε, and f were 1.2×10^{-4} Torr, 2 keV, and 1.1875 ions nm^{-2} s^{-1}, respectively, corresponding to erosive conditions for IBS of Au.[1,2,20] The mean wavelength of the beads λ_B is extracted by measuring the mean distance between adjacent beads on numerous line profiles along the ripples. Since nanobead patterns are closely packed along each ripple, λ_B can be considered the mean nanobead diameter $\overline{D}$. In order to estimate the mean length of uninterrupted nanobeads arrays, denoted by ℓ_B, this was extracted from line profiles along ripples until convergence of the mean bead length is reached. In these symbols, the subscript B refers to the bead pattern.

Figures 1(a)–1(d) show the *optimal* nanobead patterns formed by IBS normal to the surfaces of the initial ripple patterns described in Table I. The insets provide the corresponding

TABLE I. Features of initial rippled surfaces and optimal nanobead patterns after IBS normal to the former. Here, λ_R^i and W^i are, respectively, the mean ripple wavelength and surface roughness of the initial ripple pattern; T is the temperature during sputtering to fabricate initial ripple pattern, and $\overline{D}$, σ, $\overline{A}_B$, and ℓ_B are the mean bead diameter, the standard deviation of the distribution of nanobead diameters, the mean bead amplitude, and the mean length of uninterrupted nanobead arrays along each ripple of the optimal nanobead pattern. Superscript i and subscript B refer to initial ripple pattern and nanobead pattern, respectively.

	Initial ripple pattern			Optimal bead pattern				
	λ_R^i (nm)	W^i (nm)	T (K)	$\lambda_B \simeq \overline{D}$ (nm)	$\sigma/\overline{D}$	$\overline{A}_B$ (nm)	ℓ_B (μm)	Time (min)
NB(a)	27	1.1	298	36.5	0.24	1.8	0.46	10
NB(b)	30	1.8	303	47.8	0.21	3.1	>0.95	25
NB(c)	47	2.7	313	47.9	0.18	2.8	>2.5	25
NB(d)	69	1.0	333	51.3	0.20	3.0	>0.8	25

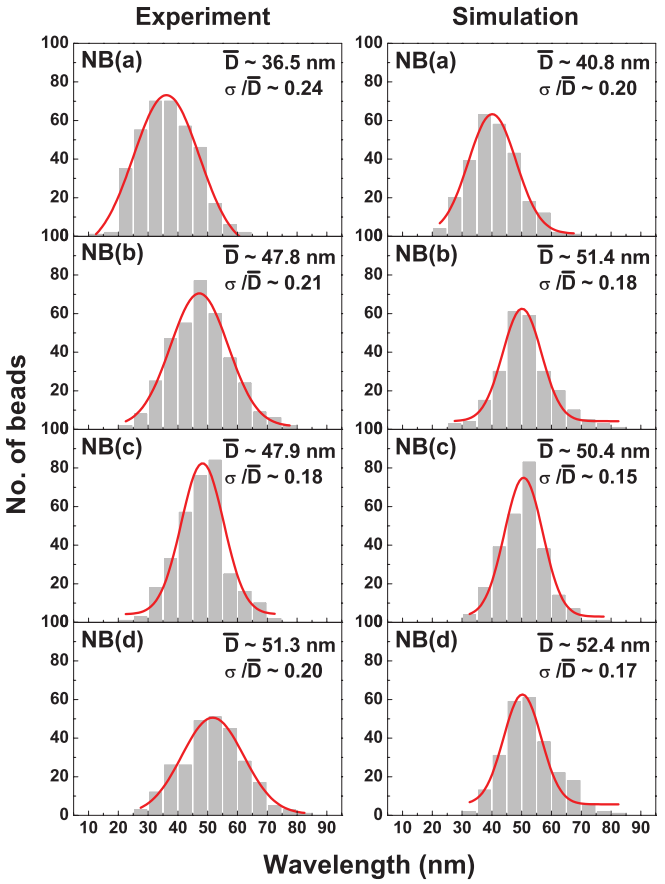

FIG. 2. (Color online) Histograms showing the distribution of the bead diameter D in each nanobead pattern at the optimal time for the (left) experimental and (right) numerical morphologies considered in Fig. 1. Solid red lines are Gaussian fits from which we estimate the standard deviations of the distributions σ, shown in Table I.

height power spectral densities (PSD; squared modulus of the Fourier transform). For each case, the latter features a line of maxima corresponding to a heterogeneous ripple structure and two additional, more diffuse peaks at 90° corresponding to the nanobead alignment along the perpendicular direction.

The optimal time when the optimal nanobead pattern forms is determined by the maximal ordering parameter, which is defined as the intensity of the first-order spot relative to that of the zeroth-order spot in the height-height correlation function of a nanobead pattern.[20] The optimal nanobead pattern concurrently shows minimal $\sigma/\overline{D}$ and maximal ℓ_B values. Here, $\sigma/\overline{D}$ is the standard deviation σ of the bead diameter D, normalized by the mean bead diameter $\overline{D}$, while σ is the standard deviation of the distribution of the bead diameters, as displayed in Fig. 2. The mean bead amplitude $\overline{A}_B$ is estimated from the distribution of the bead heights. Both distributions are obtained from numerous line profiles across nanobeads.

From Fig. 1, we can see that IBS normal to the previously rippled surface indeed leads to the production of nanobead patterns, irrespective of the rippled initial condition. Irradiation at normal incidence of a flat surface leads to formation of a *disordered* array of dots under the present conditions [see, e.g., Fig. 2(e) in Ref. 20]. For an initially rippled surface, the undulations guide dot formation with the result that nanobead patterns develop with a well-defined quasi-one-dimensional order. Note, however, that the quality of the nanobead structure at the corresponding optimal time does depend on the initial condition: for instance, the nanobead pattern obtained from the initial surface NB(a) shown in Fig. 1(a) has an inferior quality: thus, the one-dimensional (1D) order of the nanobeads is frequently interrupted by a high density of defects that induce coalescence of neighboring ripples and make the pattern look locally more similar to a quasi-two-dimensional pattern of nanodots. As indicated in Table I, the mean length of uninterrupted nanobead arrays ℓ_B is about 460 nm for NB(a), while it is larger than 800 nm for the other bead patterns. Also, $\sigma/\overline{D}$ is 0.24 for NB(a), which is noticeably larger than in the other bead patterns, where it is around 0.2, so that individual beads are more heterogeneous. For NB(a), the initial ripple size estimated by the ripple wavelength ($\lambda_R^i \simeq 27$ nm) or the global roughness ($W^i \simeq 1.1$ nm) is smaller than that of the other ripple patterns. Hence, due to the relatively small size of the ripples, the initial pattern NB(a) seems to be destroyed early by IBS normal to the rippled surface and cannot constrain the growth of individual nanobeads until the nanobead pattern fully develops over the whole rippled surface. Furthermore, at the optimal time, λ_B is still much smaller for the NB(a) case. On the other hand, the nanobead patterns developed for initial conditions with larger λ_R^i show better quasi-1D ordering, as observed in Figs. 1(b)–1(d). Moreover, they show large ℓ_B and small $\sigma/\overline{D}$ values, as summarized in Table I, supporting the idea that the initial ripple guides the growth of nanodots preferentially, with its initial wavelength value being critical to an ordered growth of the nanobeads.

Simultaneous with the dynamical process of bead formation and ordering, we can assess how the initial ripple morphology evolves under irradiation. Thus, the time evolution of the experimental λ_R and W are plotted in Fig. 3 (open symbols). As noted here, λ_R and W converge approximately to $\lambda_R^* \simeq 50$ nm and $W^* \simeq 2.25$ nm for all cases, except when the initial values are very different from the final ones or NB(a). Notice that the value of λ_R^* is quite close to those of the optimal $\lambda_B \simeq \overline{D}$ in Table I for conditions NB(b)–NB(d), the corresponding optimal times being achieved when $\lambda_B \approx \lambda_R^*$. This may explain

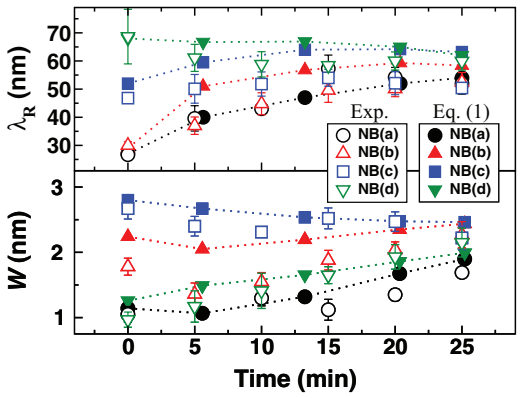

FIG. 3. (Color online) Time evolution of (top) ripple wavelength λ_R and (bottom) global roughness W for experiments (open symbols) and numerical simulations of Eq. (1) (solid symbols) for the conditions considered in Fig. 1. Lines are guides to the eye.

why the beads formed for condition NB(a) (in which the initial ripples are too narrow compared with the natural dot size $\overline{D}$) overgrow single ripples rapidly. This leads to a smaller optimal time, later deterioration of 1D order, and worse convergence to W^*, even though λ_R becomes large and finally close to λ_R^*. Generally speaking, and as seen in Fig. 3 (open symbols), it is interesting to note that the values of the ripple wavelength and roughness decrease with time for large initial value conditions. Thus, in the case of NB(d) the wavelength decreases from approximately 70 nm to a value close to λ_R^*, while for the initial rippled surface NB(c) the roughness is reduced from approximately 2.75 nm to W^*.

III. THEORETICAL DESCRIPTION AND COMPARISON WITH EXPERIMENTS

In order to understand the dynamics of nanobead pattern formation, we consider the eKS equation.[7,12] In contrast to other continuum models, it has been shown to reproduce experimental properties such as the ordering of the nanobead pattern and its long-term preservation for the case of a single initial condition.[20] This evolution equation for the height field $h(\mathbf{r},t)$ of the irradiated target reads

$$\frac{\partial h}{\partial t} = -\nu\nabla^2 h - \mathcal{K}\nabla^4 h + \lambda_1(\nabla h)^2 - \lambda_2\nabla^2(\nabla h)^2 + \eta, \qquad (1)$$

where ν, $\mathcal{K}$, λ_1, and λ_2 are *positive* coefficients depending on phenomenological parameters and η is an uncorrelated Gaussian noise modeling fluctuations in sputtering and surface relaxation events, which has zero average and correlations $\langle\eta(\mathbf{r},t)\eta(\mathbf{r}',t')\rangle = N\delta(\mathbf{r}-\mathbf{r}')\,\delta(t-t')$. The first two terms in Eq. (1) actually correspond to the classic BH model, in which the one with coefficient ν implements the unstable geometrical dependence of the local sputtering yield, while the one with coefficient $\mathcal{K}$ accounts (to linear order) for stabilizing surface-diffusion currents that can be induced both by temperature and by the ion beam.[12] To nonlinear order, the term with coefficient λ_1 in Eq. (1) is the so-called Kardar-Parisi-Zhang (KPZ) nonlinearity, which reflects the fact that, at any given surface point, erosion proceeds along the local normal direction, usually being responsible for amplitude saturation of the pattern at long times.[10] Up to this point, the equation determined by the first three terms on the right-hand side of Eq. (1) is the celebrated KS equation, which has played a relevant role in the modeling of IBS systems.[3] Finally, a distinctive feature of the eKS model, that is, of the full Eq. (1), is the conserved Kardar-Parisi-Zhang (cKPZ) term with coefficient λ_2, which describes local redeposition of sputtered material and surface-confined transport.[12] For $N = 0$, this equation has been successfully applied to describe quantitatively IBS of silicon surfaces.[24,25] Our present case of metallic targets under erosive irradiation conditions is consistent with the main physical assumptions behind the derivation in Ref. 12, with material transport reducing essentially to surface-confined currents of adatom and advacancies.[2]

Given the nonlinear nature of the eKS system, we resort to numerical simulations that follow a similar scheme to Refs. 23–25. For $N = 0$ the behavior of the equation is controlled by the single dimensionless parameter $r = \nu\lambda_2/(\mathcal{K}\lambda_1)$.[23,26] In general, the KPZ nonlinearity with coefficient λ_1 is responsible for amplitude saturation and pattern disordering at long times, while the cKPZ term favors dot coarsening and short-range order at short/intermediate times. The predominance of each nonlinearity depends on the dimensionless parameter r. Actually, small values of r imply conditions in which the effect of the cKPZ term is relatively secondary to that of the KPZ term, so that the long-time behavior expected for a *flat initial condition* is an array of dots with weak short-range order.[23,26] This is the case in the present system in which the value of this parameter that provides a good quantitative agreement with the experiments is of unit order.[20] In our case we will consider $r = 0.85$. An additional constraint that allows us to determine the values of the equation coefficients is the wavelength of the linearly most unstable mode, $\lambda_* = 2\pi(2\mathcal{K}/\nu)^{1/2} \simeq 50$ nm. Since the small noise amplitudes were proven not to significantly alter the pattern structures, the physical time and height scales can be rescaled varying $\mathcal{K}/\nu^2$ and ν/λ_1 as in Refs. 26 and 23 to heuristically obtain the parameter values leading to our most complete quantitative comparison with experimental data (see below and Figs. 1–3). These are $\nu = 12$ nm^2 min^{-1}, $\mathcal{K} = 379$ nm^4 min^{-1}, $\lambda_1 = 4.88$ nm min^{-1}, $\lambda_2 = 132$ nm^3 min^{-1}, and $N = 5$ nm^2 min$^{-1/2}$. Note that the present parameter choice is much more involved than in previous studies for initially flat Si targets.[24,25] This is due to the availability of approximate analytical results relating features of the solutions for flat initial conditions with equation parameters, as shown in Refs. 23 and 26, which do not apply in the present case. Additionally, we have checked the robustness of this parameter set, verifying that small changes in their values do not modify substantially the results to be discussed below.

For a flat initial condition, at short times Eq. (1) leads to the formation of a disordered array of dots due to a morphological instability controlled by the linear terms. Thus, sinusoidal perturbations of a flat profile with wavelengths $\lambda > \lambda_c = 2\pi(\mathcal{K}/\nu)^{1/2} \simeq 35$ nm are amplified with time, while those with $\lambda < \lambda_c$ are damped out. The specific perturbation with $\lambda = \lambda_*$ grows at a maximum rate and provides the size of the linear dot pattern. One might expect that the effective coarsening of λ_R seen in experiments (Fig. 3, open symbols, top panel) for rippled initial conditions with $\lambda_R^i < \lambda_c$ might be due to this linear filtering of small-wavelength components of the surface morphology. Thus, it is interesting to elaborate on this possibility in detail since analytical solutions become available.

A. Linearized eKS equation

If one sets nonlinearities to zero in the eKS equation (BH limit), the space Fourier modes $h_{\mathbf{k}}(t)$ of the height field behave independently of one another, as $h_{\mathbf{k}}(t) = h_{\mathbf{k}}(t = 0)\exp(\omega_k t) + \hat{h}_{\mathbf{k}}(t)$, where $\hat{h}_{\mathbf{k}}(t) = \int_0^t e^{\omega_k(t-\tau)}\,\eta_{\mathbf{k}}(\tau)\,d\tau$ is the solution for a flat initial condition and

$$\omega_k = \nu k^2 - \mathcal{K}k^4 \qquad (2)$$

is the so-called dispersion relation, which is a function of the magnitude of the wave vector, $k = |\mathbf{k}|$, only. Under conditions for pattern formation in which $\nu,\mathcal{K} > 0$, there is a finite band of (unstable) Fourier components whose amplitude grows exponentially, which are those for which $\omega_k > 0$, namely, $k < k_c = (\nu/\mathcal{K})^{1/2}$. Using the relation $\lambda = 2\pi/k$ between

wave vector k and wavelength λ, the unstable wavelengths verify $\lambda > \lambda_c = 2\pi/k_c \simeq 35$ nm for the chosen values of the equation coefficients. Therefore, the surface amplitude will evolve differently for surfaces that are initially prepared as sinusoidal ripples with different wave vectors: ripples for which the wavelength is smaller than λ_c will, in principle, decay, while the amplitude of ripples with wavelength larger than λ_c will increase, at least until nonlinear effects set it. Among these unstable modes there is a unique value $k = k_*$ that corresponds to a maximum growth rate, i.e., for which ω_k takes on its maximum positive value. For flat initial conditions, a disordered dot structure would develop, with a typical dot size equal to $\lambda_* = 2\pi/k_* = \sqrt{2}\lambda_c \simeq 50$ nm. These features can be appreciated in Fig. 4.

We employ the same symbol and color coding as in previous figures. Namely, we use the open symbols joined with dashed lines for a sinusoidal ripple condition that has the same *mean* values of roughness and wavelength as the experimental initial condition. When we perform numerical simulations using experimental images as initial conditions, we employ solid symbols and solid lines. We should note that the difference between the initial values of the roughness and wavelength in these simulations and those given in Table I is because the latter are average values.

From Fig. 4 it is clear that for sinusoidal initial conditions the amplitude, and therefore the roughness, decays at short times provided $\lambda_R^i < \lambda_c$, as for conditions NB(a) and NB(b) when $\lambda_R^i = 27$ and 30 nm, respectively. On the other hand, the ripple amplitude is amplified if $\lambda_R^i > \lambda_c$, as for conditions NB(c) and NB(d) when $\lambda_R^i = 47$ and 69 nm, respectively, with the amplification rate being larger for values closer to λ_*. For initial conditions NB(a) and NB(b), in the stable band of modes, the increase of the roughness for sufficiently long times may seem unexpected. In order to understand it, note that we are considering an isotropic (BH) equation, which for a flat initial condition is well known to lead to a disordered array of dots (beads). Thus, simultaneous with the evolution of the rippled initial condition, some contribution to dot formation and dynamics is to be expected. This is substantiated by the exact solution of the linearized eKS equation, which for the

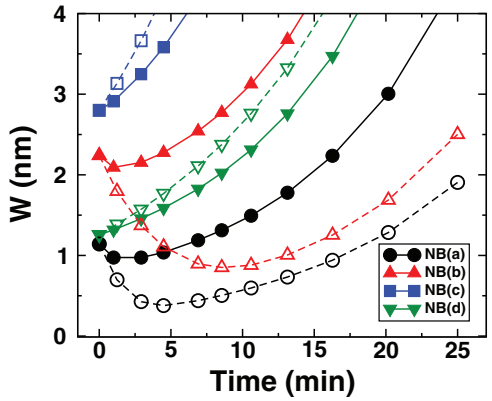

FIG. 4. (Color online) Time evolution of $W(t)$ as obtained from numerical simulations of the linearized eKS (BH) equation using sinusoidal initial conditions (dashed lines and open symbols) or experimental initial conditions (solid lines and solid symbols) as in Table I. Lines are guides to the eye.

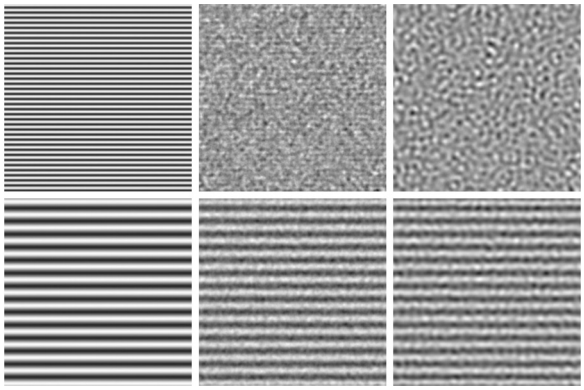

FIG. 5. Surface morphologies (top views) as predicted by the linearized eKS (BH) equation using sinusoidal initial conditions for cases (top) NB(a) and (bottom) NB(d) in Table I for times $t = 0$,6, and 25 min from left to right. The size of each image is 1×1 μm^2.

surface roughness readily leads to[27]

$$W^2(t) = W^2_{\text{flat}}(t) + \int e^{2\omega_k t}\, \langle h_{\mathbf{k}}(t=0) h_{-\mathbf{k}}(t=0)\rangle\, d\mathbf{k}, \qquad (3)$$

where $W^2_{\text{flat}}(t) = \int N\,(1 - e^{2\omega_k t})/(-2\omega_k)\, d\mathbf{k}$ is the roughness for a flat initial condition (where N is the noise amplitude) and the integrals extend over all wave-vector values. For a purely sinusoidal initial condition, only one value of $\mathbf{k}$ contributes to the second term on the right-hand side of Eq. (3), and such a contribution decays exponentially with time if the initial condition is in the stable Fourier band. Thus, the increase of $W(t)$ seen in Fig. 4 for sinusoidal conditions NB(a) and NB(b) can be attributed to the first term in Eq. (3). Namely, the short-time dynamics wipes out the initial ripple efficiently, and for longer times the evolution occurs as for a flat initial condition: a disordered dot structure forms with dot size close to λ_*, and the roughness increases. This behavior can be appreciated in Fig. 5, in which we show the evolution of the surface morphology using sinusoidal conditions for cases NB(a) (top row) and NB(d) (bottom row) for times $t = 0$,6, and 25 min from left to right.

The behavior we have just described is clear for condition NB(a). However, for condition NB(d), the initial surface mode is well into the unstable band, so that the initial ripple amplitude increases very fast and noise contributions [dominant, e.g., for the NB(a) condition at $t = 25$ min] have a mild effect, reduced to a slight disordering of the ripple shapes.

The time evolution of the experimental initial conditions which are not purely sinusoidal is more complex but can still be rationalized with the help of this linear argument. Any initial condition can be thought of as a superposition of sinusoidal components. The early time dynamics works as a low-pass filter in the sense that components with $k > k_c = 2\pi/\lambda_c$ are damped out, while long-wavelength components are amplified. With solid lines and solid symbols in Fig. 4, we show the evolution of the roughness for the linearized eKS equation using as initial conditions experimental topographies corresponding to the four conditions in Table I. For $\lambda_R^i > \lambda_c$, the behavior of $W(t)$ does not differ much from that obtained for the corresponding sinusoidal initial condition (dashed lines and open symbols), with larger differences being obtained for

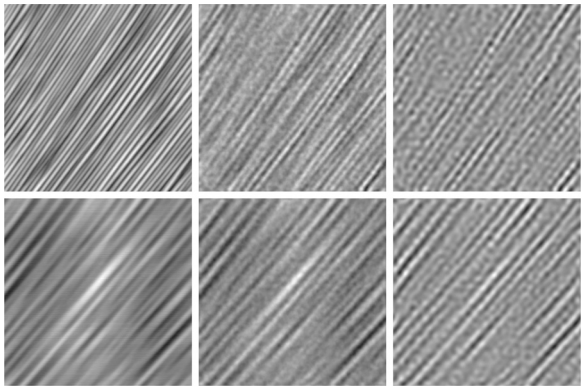

FIG. 6. Surface morphologies (top views) as predicted by the linearized eKS (BH) equation using experimental initial conditions for cases (top) NB(a) (upper row) and (bottom) NB(d) in Table I for times $t = 0$,6, and 25 min from left to right. The size of each image is $1 \times 1\ \mu\text{m}^2$.

cases in which $\lambda_R^i < \lambda_c$. The analysis of the topographies is perhaps even more informative. We provide examples in Fig. 6 for conditions NB(a) and NB(d) in Table I. By inspecting Fig. 6, we can see that, irrespective of the wavelength of the initial condition, small wavelength components are damped out during the evolution, leading to a morphology dominated by a ripple structure with a wavelength that is comparable to λ_*. Notice there is a faint formation of dots ("beads") along the directions of some of the initial ripples. However, the roughness of these morphologies increases exponentially fast, as shown in Fig. 4, and it does not show the convergence seen in experiments to a similar value independently of the initial conditions (see bottom panel in Fig. 3, open symbols). The ripple wavelength does not evolve in a similar way to the experimental one either (compare the top panel in Fig. 3, open symbols, with Fig. 7). Indeed, while the decoupling of Fourier modes hinders the linearized eKS equation from reproducing ripple coarsening for purely sinusoidal initial conditions, an effective coarsening due to the mentioned low-pass-filtering effect can occur for initial conditions that are a superposition of sine waves, as seen in Fig. 7. Note also that, for experimental conditions NB(c) and NB(d) in which the initial surface has little contribution from short-wavelength components, such a low-pass-filtering process is essentially nonoperative because there is no evolution of the ripple wavelength, as suggested by the bottom row in Fig. 6. This contrasts the behavior of $\lambda_R(t)$ seen in experiments for such initial conditions, justifying the need for nonlinear terms in the interface equation.

B. Full eKS equation

As we have just seen, the linearized eKS equation does not lead to bead formation for any initial condition that is a pure sine wave. Even taking as initial conditions for the simulations the experimental rippled surfaces corresponding to Table I, the surface roughness still does not show the type of convergence observed in the experiments (see bottom panel of Fig. 3, open symbols). Thus, nanobead formation and alignment, concurrent with convergence of $\lambda_R(t)$, need take place through nonlinear effects, and one should consider the full eKS equation to reproduce the experiments. In order to understand the interplay of nonlinearities in Eq. (1), it is natural to first consider the dynamics for patterned initial surfaces with a purely sinusoidal shape. As seen in Fig. 8, a bead structure does emerge at long times, whose ordering depends sensitively upon the wavelength of the initial condition. Still, sinusoidal initial conditions do not allow for quantitative agreement between experiments and simulations. This is readily seen when comparing the bottom panel of Fig. 3 (open symbols) with Fig. 9, where we show the dynamics of $W(t)$ (dashed lines and open symbols) for sinusoidal initial ripples with the same wavelength and average roughness as the experimental conditions in Table I. In any case, by comparing Fig. 9 (full eKS equation) with Fig. 4 (linearized eKS equation), the former supports the importance of nonlinear effects even at small times.

A more successful description is obtained when the initial conditions are taken from the experimental topographies. Thus, in contrast to the sinusoidal conditions, the evolution of $W(t)$ is now quite similar to that in experiments (compare Fig. 9 with the bottom panel in Fig. 3, open symbols). Movies of the full simulated surface dynamics are available in the Supplemental Material[28] for the four experimental initial conditions, where the nontrivial interplay between the two

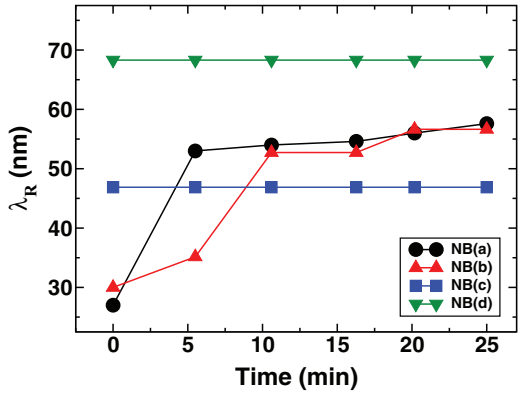

FIG. 7. (Color online) Time evolution of λ_R as obtained from numerical simulations of the linearized eKS (BH) equation using experimental initial conditions as in Table I. Lines are guides to the eye.

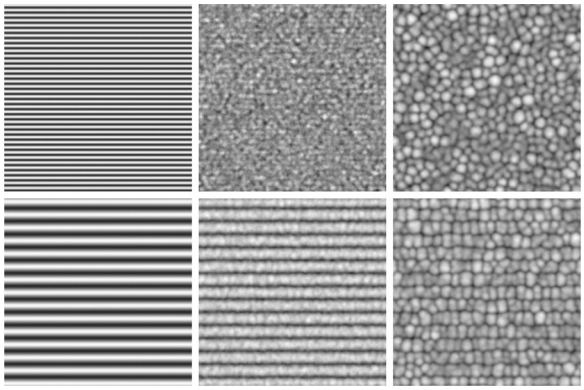

FIG. 8. Surface morphologies (top views) as predicted by the full eKS equation using sinusoidal initial conditions for cases (top) NB(a) and (bottom) NB(d) in Table I for times $t = 0$,6, and 25 min from left to right. The size of each image is $1 \times 1\ \mu\text{m}^2$.

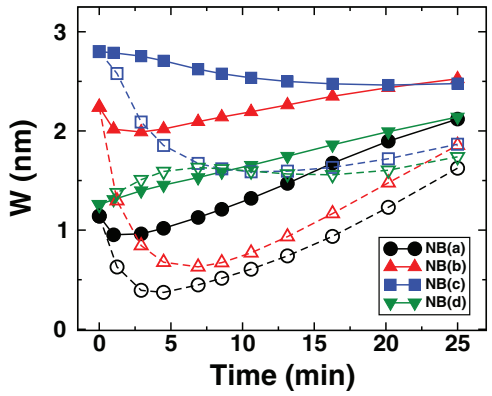

FIG. 9. (Color online) Time evolution of $W(t)$ from numerical simulations of Eq. (1) using sinusoidal initial conditions (dashed lines and open symbols) and experimental initial conditions (solid lines and symbols) as in Table I. Lines are guides to the eye.

length scales, λ_R and the bead size λ_B, can be appreciated. The final morphology reached in each case is compared in Fig. 1 (bottom row) with the corresponding experimental topography at the optimal time (top row); agreement is noticeable, including the behavior of the corresponding PSD functions. As in the experiments, the simulated ripple wavelength curves $\lambda_R(t)$ converge to a value close to λ_* (compare the top panel in Fig. 3), while a bead structure sets in along the ripple directions developing short-range order. Disorder in the bead structure [see, for example, condition NB(a) for long times] occurs for small λ_R^i, so individual ripples cannot constrain bead overgrowth. In view of the compactness of the eKS equation as a model for the present complex pattern formation process, we believe the agreement with experiments is rather satisfactory; additional features, such as the bead size distribution (see Fig. 2), support this conclusion.

IV. SUMMARY AND CONCLUSIONS

In our nanobead pattern formation experiments, a dynamical regime is reached in which the values of the global roughness and the wavelength of the remaining undulations are largely independent of those prior to bombardment. Specifically, the value for λ_R "selected" by the dynamics is close to the size of the dots that would be produced on an initially flat surface, keeping all other experimental conditions fixed. The initial ripples play the role of a template that guides dot alignment, leading to arrays of nanobeads. The final 1D order worsens for surfaces in which the initial ripple wavelength and roughness differ significantly from the converged values. Note that the hierarchical nanobead pattern does not require secondary morphological transitions as in other pattern-forming systems far from equilibrium.[29] Its complex morphology arises, rather, from the interplay between two basic structures, i.e., the initial ripples and the dots produced at normal incidence. From a practical point of view, the advantage is that both are controlled by a single technique and a common set of physical parameters.

In order to elucidate the processes driving the dynamics of the nanobead structure, we have performed simulations of the eKS equation. Although more refined models can be considered that are sensitive to, e.g., the specifics of surface diffusion for metallic systems, the quantitative agreement of Eq. (1) with the main features of the experimental patterns is substantial. Physically, this fact stresses the relevance of relaxation processes that preserve the amount of material, such as surface-confined transport due to local redeposition. Technically, it reflects in the non-negligible effect of the conserved KPZ term, even if the numerical value of λ_2 is relatively small. Note that the KS equation, which is obtained for $\lambda_2 = 0$ in Eq. (1), is known not to reproduce nanobead alignment.[20]

From a general point of view of modeling pattern dynamics at surfaces, our simulations underscore the crucial role for the evolution that is played by the spatial correlations that exist in the initial morphology. For applications of the present nanostructuring technique, one should take into account this fact if interested in producing surface morphologies with prescribed topographical properties. For instance, in our case an initial rippled surface with a wavelength and roughness that are similar to the final ones will accelerate nanobead alignment, with maximal order and minimal defects in the resulting structure.

ACKNOWLEDGMENTS

This work was supported by NRF (Korea) Grant No. 20100010481 by MICINN (Spain) Grant No. FIS2009-12964-C05-01 and by MEC (Spain) Grants No. FIS2012-32349 and No. FIS2012-38866-C05-01. J.M.-G. was supported by MICINN (Spain) under the Juan de la Cierva program.

*jskim@sm.ac.kr
†cuerno@math.uc3m.es

[1] U. Valbusa, C. Boragno, and F. Buatier de Mongeot, J. Phys. Condens. Matter **14**, 8153 (2002).
[2] W. L. Chan and E. Chason, J. Appl. Phys. **101**, 121301 (2007).
[3] See the special section on Surface nanopatterns induced by ion-beam sputtering in J. Phys. Condens. Matter. **21**, 220301–224026 (2009).
[4] S. Rusponi, G. Costantini, C. Boragno, and U. Valbusa, Phys. Rev. Lett. **81**, 4184 (1998).
[5] S. Facsko, T. Dekorsy, C. Koerdt, C. Trappe, H. Kurz, A. Vogt, and H. L. Hartnagel, Science **285**, 1551 (1999).
[6] J. A. Sánchez-García, L. Vázquez, R. Gago, A. Redondo-Cubero, J. M. Albella, and Z. Czigany, Nanotechnology **19**, 355306 (2008).
[7] T. C. Kim, C.-M. Ghim, H. J. Kim, D. H. Kim, D. Y. Noh, N. D. Kim, J. W. Chung, J. S. Yang, Y. J. Chang, T. W. Noh, B. Kahng, and J.-S. Kim, Phys. Rev. Lett. **92**, 246104 (2004).
[8] G. Costantini, F. Buatier de Mongeot, C. Boragno, and U. Valbusa, Phys. Rev. Lett. **86**, 838 (2001).
[9] R. M. Bradley and J. M. E. Harper, J. Vac. Sci. Technol. A **6**, 2390 (1988).
[10] M. A. Makeev, R. Cuerno, and A.-L. Barabási, Nucl. Instrum. Methods Phys. Res., Sect. B **197**, 185 (2002).
[11] S. Facsko, T. Bobek, A. Stahl, H. Kurz, and T. Dekorsy, Phys. Rev. B **69**, 153412 (2004).

[12]M. Castro, R. Cuerno, L. Vázquez, and R. Gago, Phys. Rev. Lett. **94**, 016102 (2005).
[13]M. Castro and R. Cuerno, Appl. Surf. Sci. **258**, 4171 (2012), and references therein.
[14]G. Carter, Vacuum **77**, 97 (2004); **79**, 106 (2005).
[15]S. Vogel and S. J. Linz, Phys. Rev. B **75**, 085425 (2007); **75**, 155417 (2007).
[16]M. Joe, C. Choi, B. Kahng, and J.-S. Kim, Appl. Phys. Lett. **91**, 233115 (2007).
[17]J.-H. Kim, M. Joe, S.-P. Kim, N.-B. Ha, K.-R. Lee, B. Kahng, and J.-S. Kim, Phys. Rev. B **79**, 205403 (2009).
[18]A. Keller and S. Facsko, Phys. Rev. B **82**, 155444 (2010).
[19]J. Völlner, B. Ziberi, F. Frost, and B. Rauschenbach, J. Appl. Phys. **109**, 043501 (2011).
[20]J.-H. Kim, N.-B. Ha, J.-S. Kim, M. Joe, K.-R. Lee, and R. Cuerno, Nanotechnology **22**, 285301 (2011).
[21]T. Yasseri and R. Kree, Nucl. Instrum. Methods Phys. Res., Sect. B **268**, 2496 (2010).
[22]G. M. Whitesides and M. Boncheva, Proc. Natl. Acad. Sci. USA **99**, 4769 (2002).
[23]J. Muñoz-García, R. Cuerno, and M. Castro, J. Phys. Condens. Matter **21**, 224020 (2009).
[24]J. Muñoz-García, R. Gago, L. Vázquez, J. A. Sánchez-García, and R. Cuerno, Phys. Rev. Lett. **104**, 026101 (2010).
[25]J. Muñoz-García, R. Gago, R. Cuerno, J. A. Sánchez-García, A. Redondo-Cubero, M. Castro, and L. Vázquez, J. Phys. Condens. Matter **24**, 375302 (2012).
[26]J. Muñoz-García, R. Cuerno, and M. Castro, Phys. Rev. E **74**, 050103(R) (2006).
[27]T. J. da Silva and J. G. Moreira, Phys. Rev. E **56**, 4880 (1997).
[28]See Supplemental Material at http://link.aps.org/supplemental/10.1103/PhysRevB.87.085438 for movies of the evolutions described by the full eKS equation for experimental initial conditions.
[29]M. Cross and H. Greenside, *Pattern Formation and Dynamics in Nonequilibrium Systems* (Cambridge University Press, Cambridge, 2009).